All-Epitaxial Bulk Acoustic Wave Resonators

Jeffrey Miller,* John Wright, Huili Grace Xing, and Debdeep Jena

There is a growing interest in the exploration of the nitride material family for radically scaled, high frequency, ultrasonic devices by epitaxial growth techniques. Furthermore, the introduction of epitaxial growth techniques to conventional nitride-based acoustic technology opens the door to exciting new families of structures for phonon confinement. As the need for higher frequency communications increases, both piezoelectrics and electrodes must scale to smaller dimensions. It has recently become possible to epitaxially grow single-crystalline, wurtzite AlN/NbN piezoelectric/metal heterostructures. The epitaxial NbN films maintain high crystalline quality and electrical conductivity down to several nanometers thickness. This study demonstrates preliminary results on the feasibility of an all-epitaxial bulk acoustic wave technology by growing and characterizing the radio frequency (RF) properties of an epitaxial AlN/NbN heterostructure.

1. Introduction

AlN has long proven to be a functional and formidable electromechanical material. Due to its high piezoelectricity ($e_{33} \approx 155\,\mu C\,cm^{-2}$) among semiconductors, high thermal conductivity ($\approx 340\,W\,mK^{-1}$), dielectric breakdown ($E_g \approx 6\,eV$), and manufacturability, AlN has delivered high-performing, small form factor, radio frequency (RF) filters in the form of surface acoustic wave (SAW) and bulk acoustic wave (BAW) technology. At the heart of each bulk acoustic filter, individual BAW resonators are strung together (typically in ladders or stacked configurations) to achieve bandpass operation.[1] In such resonators, the resonance frequency f_0 is inversely proportional to the length of vibrational confinement, L. Hence $f_0 \approx v_s/2\,L$, where v_s is the sound velocity in the material.[2] In AlN, the sound velocity of bulk longitudinal acoustic waves along the c-axis is about $11\,000\,m\,s^{-1}$. As the need

for higher frequency communication channels increases, it becomes critical to maintain high piezoelectric film quality as thicknesses are scaled-down into the nanoscale regime.

Progress in both AlN and GaN has sparked interest in whether epitaxial growth techniques can be harnessed for performance gains over conventional sputtering technology,[3,4] where such epitaxial films maintain their crystallinity down to the nanometer scale.[5] Furthermore, as research in acoustic technology moves to higher frequencies, the underlying phonon–phonon scattering mechanisms in attenuation transitions—dubbed the Landau–Rumer regime—as the frequency of operation exceeds a characteristic lifetime associated with the background population of thermal phonons. In this regime, the f^*Q product increases linearly with frequency.[6,7] Notably, the work in ref. [7] suggests the transition to the Landau–Rumer regime occurs earlier with increasing thermal conductivity—of high interest to the power-handling capabilities of acoustic technology.

Recently, it has been shown that single-crystalline wurtzite AlN can be epitaxially grown on compound nitride metals (e.g., NbN) on SiC by molecular beam epitaxy (MBE).[8] With the in-plane lattice parameters of (111) NbN, (0001) AlN, and SiC matched to within 1%, the possibility of an all-epitaxial BAW filter emerges—utilizing epitaxial NbN as the electrodes. To obtain higher frequency BAW devices, the electrode thickness must be scaled proportionally with piezoelectric thickness to avoid significant reduction in operation frequency and electromechanical coupling.[9] For common BAW metals, the optimum electrode thickness is about 5–10% of the piezoelectric layer thickness.[10] An epitaxial metal, such as NbN, will remain smooth, highly crystalline, electrically conducting down to a thickness of several nanometers at room temperature, and superconducting below its critical temperature $T_c \approx 10$–$16\,K$.[11,12] Thus, it is worth exploring NbN as an epitaxial electrode to potentially scale the dimensions of BAW resonators aimed at higher frequencies, and to explore fundamental physical interactions between superconductors and nanomechanical resonators. This report highlights progress in the design and fabrication toward an all-epitaxial BAW resonator, utilizing epitaxial AlN as the piezoelectric and epitaxial NbN as an electrode.

2. BAW Resonator Growth and Fabrication

The AlN/NbN epitaxial structures were grown by plasma-assisted MBE on 500 um thick semi-insulating 6H–SiC substrates, at

J. Miller, Dr. H. G. Xing, Dr. D. Jena
Department of Electrical and Computer Engineering
Cornell University
Ithaca, NY 14853, USA
E-mail: jpm433@cornell.edu

J. Wright, Dr. H. G. Xing, Dr. D. Jena
Department of Material Science and Engineering
Cornell University
Ithaca, NY 14853, USA

Dr. H. G. Xing, Dr. D. Jena
Kavli Institute for Nanoscale Science
Cornell University
Ithaca, NY 14853, USA

The ORCID identification number(s) for the author(s) of this article can be found under https://doi.org/10.1002/pssa.201900786.

substrate temperatures of 1200 and 1000 °C for NbN and AlN, respectively. Growth rates of 1–2 nm min^{-1}, and 6 nm min^{-1} were observed for NbN and AlN, respectively. For the devices in this study, the MBE-grown stack consists of a ≈330 nm AlN piezoelectric layer and a ≈24 nm NbN electrode. The rocking curve full-width at half maximum (FWHM), as characterized by X-ray diffraction, shows that the AlN on NbN was highly oriented. A FWHM of 0.25° at the (002) reciprocal lattice point was measured (**Figure 1**a). For comparison, AlN deposited by conventional sputtering techniques on typical metals yields FHWM ≈1° in micron thick films.[10] Atomic force microscopy (AFM) scans of the AlN surface after growth shows a smooth surface, with a root-mean-square (RMS) roughness of ≈0.9 nm over a 10 um × 10 um region (Figure 1b).

MBE-grown AlN/NbN stacks on 6H–SiC substrate are fabricated into single BAW resonators by standard i-line photolithography. The resonator test structure is shown in **Figure 2**. The design allows for small signal excitation of bulk longitudinal acoustic waves in AlN via RF probes. During the fabrication process, Pt was sputtered as a top electrode (shown in pink in Figure 2a). The ground plane was formed from the underlying epitaxial NbN layer (shown in red in Figure 2a). The active area was then defined as the region in which the Pt signal line overlaps the buried NbN (shown in green in Figure 2a).

Following epitaxial growth, a Cl- and Ar-based inductively coupled plasma-reactive ion etch (ICP-RIE) was used to define individual device mesas. No significant etching of the underlying SiC substrate was observed. A second, subsequent, etch was used to access the underlying NbN. Initial attempts to access the buried NbN layer via ICP-RIE etching revealed poor etch selectivity: the observed AlN etch rate was ≈1 nm s^{-1}, whereas the epitaxial NbN layer etched at ≈2–4 nm s^{-1} under the same conditions. To overcome the lack of selectivity, a two-step etch was used to access the buried epitaxial NbN layer (schematically shown in **Figure 3**a). First, the same ICP-RIE etch was timed to remove only ≈200 nm of AlN. The remaining ≈130 nm of AlN was then removed using a dilute KOH wet etch, in the photolithographic developer AZ400K, at room temperature in under 5 min.

Optical microscope images of the exposed NbN surface after exposure to the KOH etch (Figure 3b,c), show that the AlN was etched fairly uniformly over the size of the contact. Little lateral etching of the AlN was observed visually, compared with the size of the remaining AlN mesa. No visible etching of NbN occurred, as verified by profilometry. As the NbN is thick enough to remain highly reflective, and the 6H–SiC substrate is optically transparent, exposed NbN appears highly reflective under bright field illumination, and strongly blocks backside illumination. The uniformity and speed of the etch in room temperature dilute KOH indicates that the epitaxial AlN layer is N-polar. The favorable condition for wet-etching of N-polar AlN arises because KOH simultaneously serves as a catalyst in the oxidation of N-polar AlN and as a solvent for the Al_2O_3 product.[13,14] The growth of N-polar AlN on NbN by MBE was also directly observed by transmission electron microscopy.[12]

Next, 30 nm of Cr, 100 nm of Au, and 20 nm of Ti were deposited via electron beam evaporation directly on top of the exposed NbN (near the ends of the orange cutline in Figure 2b,c) to thicken the pad for RF probe placement, and protect the NbN from subsequent etches. A 350 nm tall SiO_2 support was deposited by plasma-enhanced chemical vapor deposition (at 350 °C) and patterned by an F-based ICP-RIE. This layer prevented shorting of the signal line to the underlying epitaxial NbN layer. A 20 nm Pt/10 nm Ti layer was then sputtered on top of the AlN, and along the SiO_2 support (along the red cutline shown in Figure 2b,c), serving as the signal line and top electrode of the BAW resonators. In the future, this layer can be replaced by an epitaxial NbN layer. A brief exposure to tetramethylammonium hydroxide (TMAH)-based photolithographic developer AZ726, used in preparing the photomask for deposition of the top electrode, etched the exposed AlN active area nonuniformly, forming ≈20 nm deep pits on the surface. Hence, the sputtered Pt on the active area shown in Figure 2a–c is quite rough and nonuniform. The etching of AlN in TMAH-based solvents is a well-known process in the microelectromechanical systems community; however, the degree of etching may depend on the crystalline quality.[15,16] Prior to signal line deposition, the AlN had not been exposed to any developer. A final 100 nm Pt sputter deposition near the ends of the signal line, extending up to the active area (but not including), was used to thicken the pad for RF probe placement, and planarize to the height of the ground pads.

3. BAW Resonator RF Response

Scattering parameters of the epitaxial BAW resonators were measured on an HP8722ES vector network analyzer. **Figure 4**a shows
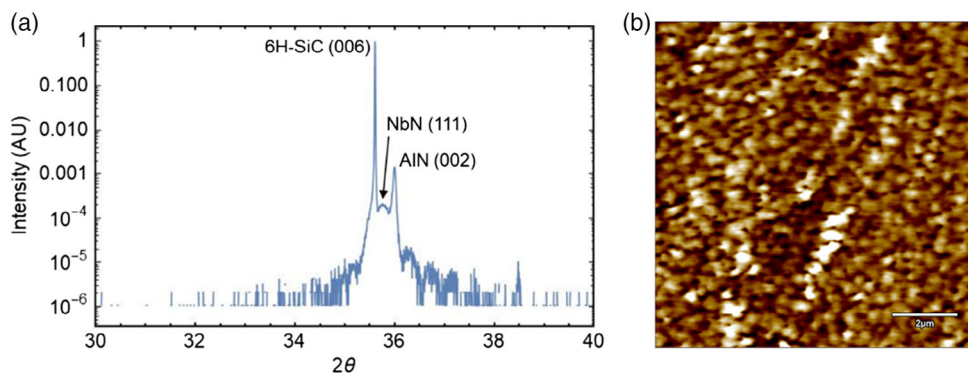

Figure 1. a) (002) X-ray diffraction rocking curve FWHM shows the AlN on NbN is highly oriented, with a FWHM 0.25°. b) AFM Surface Height Map over a 10 um × 10 um region showing a smooth AlN surface after MBE-growth, with RMS roughness ≈0.9 nm.
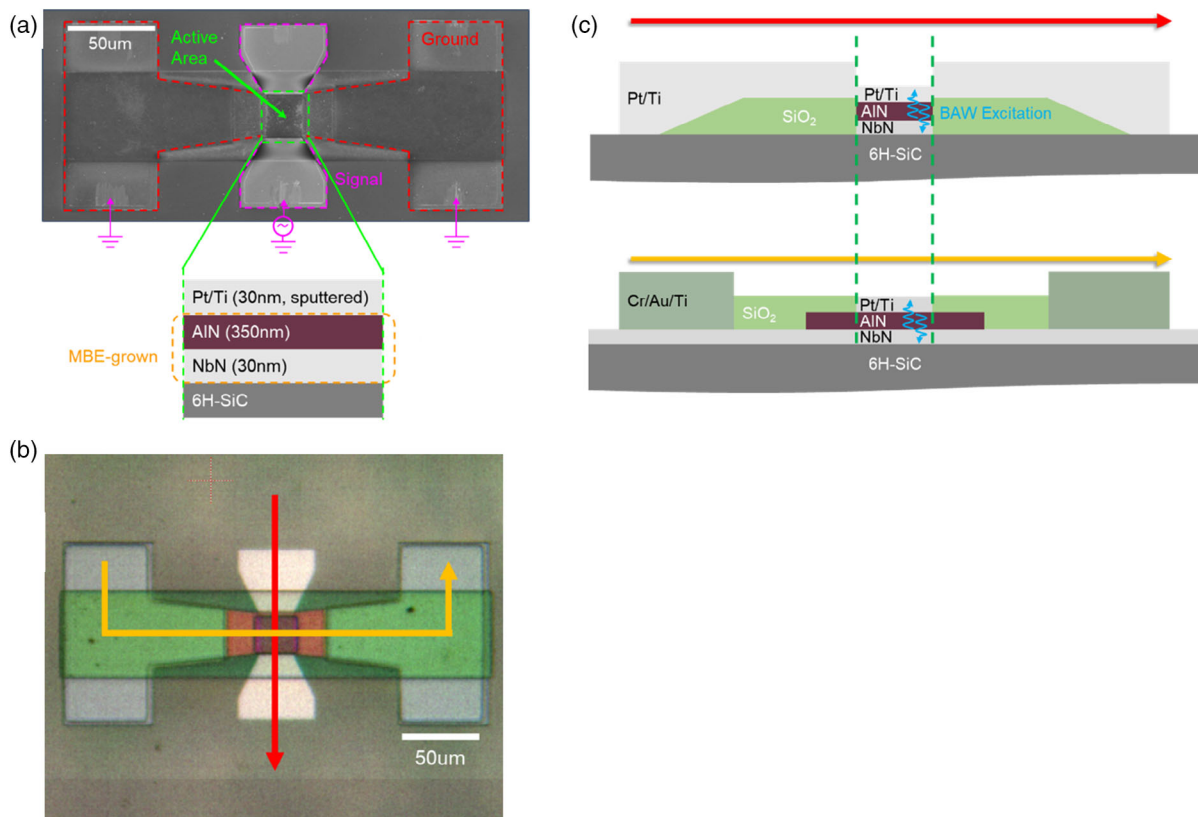
Figure 2. a,b) Top-down scanning electron microscope (SEM) and optical microscope images of the same mounted Pt/AlN/NbN resonator. The design allows for small signal excitation of bulk longitudinal acoustic waves in AlN via RF probes. The active area is defined as the region in which the Pt signal line overlaps the buried NbN. In the particular device shown, this area forms a rectangle of about 1000 um². c) Schematic depiction of the completed resonator along the red and orange cutlines shown in (b). Prior to signal line deposition, the necessary exposure to photolithographic developer damaged the exposed AlN surface. Hence, the sputtered Pt on the active area shown in (a) and (b) is quite rough. This problem could be avoided in the future by growing NbN directly on top of the AlN, simultaneously passivating the AlN surface and serving as a top electrode.

the return loss of a single BAW resonator (blue curve), with an active area of $\approx 1000 \, um^2$. Oscillatory fringes were also observed in the reflection coefficient, S_{11}, extending from roughly 3–16 GHz, which are attributed to longitudinal BAW excitation within the AlN layer modulated by thickness modes of the 6H–SiC substrate later in this section. On-wafer short devices, in which the AlN cavity had been etched out and filled with Pt, were used to determine the resistance and inductance of the surrounding metallization. A series RL circuit fit to the S_{11} response of the short devices, revealed the inductance (L) and resistance (R) of the surrounding metallization to be 36 pH and resistance to be 10 Ω, respectively. The series resistance, which includes the underlying NbN layer, agrees well with some of the best resistivities in this study. Current NbN films in this study achieved a bulk resistivity as low as 29.0 μΩ cm, and 34.0 μΩ cm in ref. [12] for a 35 nm thick film. This is higher than the bulk resistivity of other common BAW electrodes such as Pt (10 μΩ cm), Mo (5 μΩ cm), Al (2.65 μΩ cm) and could be lowered with further growth studies.

However, DC current–voltage measurement scans across the top electrode of the resonators revealed the 30 nm top Pt electrode to be as large as 100 Ω, and vary across devices. This additional resistance was attributed to the unintentionally roughened

AlN surface prior to metal deposition described in the previous section, which was not present in the short devices because the AlN was removed prior to metal deposition. With the roughness on order of the target Pt thickness, the top electrode was somewhat discontinuous, and consequently more resistive. Hence, a large portion of the return loss was attributed to the charging and discharging of the resistive Pt electrodes.

Before considering the electromechanical response of the resonator stack, an RLC circuit was used to characterize the effect the inductance (L) of the surrounding metallization and high electrode resistance play on the measured reflection coefficient, S_{11}. For frequencies that are off-resonance, the resonator is well represented by a capacitor, in series with the electrode resistance, and inductance of surrounding metallization. A least-squares fit to S_{11} was used to extract an electrode resistance (R) and electrostatic capacitance (C), associated with the charge storage capability of the top and bottom electrodes from susceptibility alone. For the device shown in this work, the extracted electrode resistance and electrostatic capacitance were 75 Ω and 0.3 pF (a reasonable parameter considering the area and dimensions of the AlN cavity), respectively. The return loss of this RLC system, defined as $RLC_{electrode}$ shown in green in Figure 4a, was then calculated from the reflection coefficient (S_{11}) of the electrode resistance,
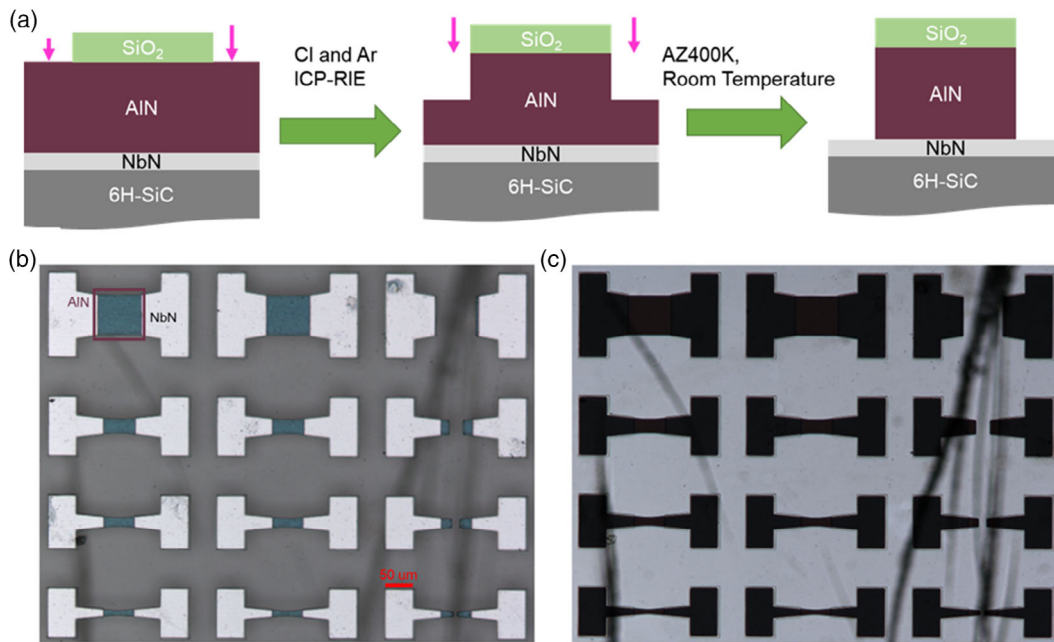
Figure 3. a) Schematic depiction of two-step etch process utilized in this work to access the buried NbN. An initial Cl and Ar-based ICP-RIE etch removed about 200 nm of AlN. The remaining AlN was removed via a 5 min etch in AZ400K at room temperature, whereas the NbN remained undamaged. b,c) Bright-field and dark-field optical microscope images of the device mesas after the AZ400K dip. As the NbN is thick enough to remain highly reflective, and the 6 H–SiC substrate is optically transparent, exposed NbN appears highly reflective under bright-field illumination, and strongly blocks illumination under dark-field illumination.
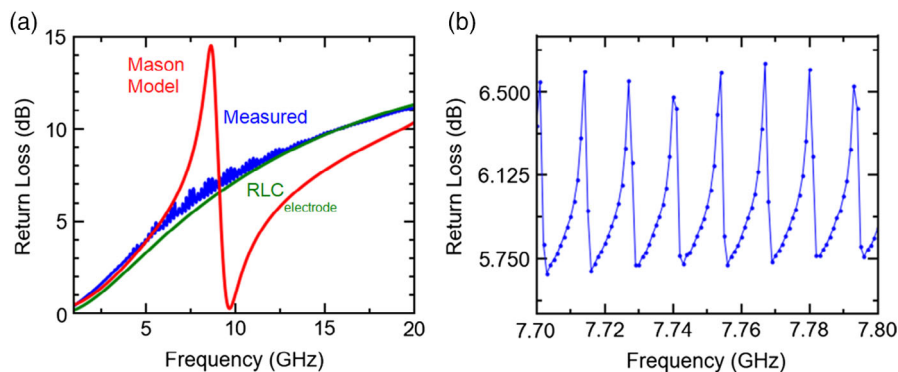

Figure 4. a) Measured return loss of a Pt/AlN/NbN BAW resonator (1000 um^2) shown in blue. The oscillatory fringes observed in the return loss, beginning around 3 GHz, are attributed to longitudinal BAW excitation in the AlN layer which are then modulated by 6 H–SiC substrate thickness-modes. A large portion of energy is spent charging/discharging of the damaged Pt electrodes, and is modeled by calculating the reflection coefficient of the shunt electrode resistance (75 Ω), electrostatic capacitance of the resonator (0.3 pF), and inductance of surrounding metallization (36 pH). This purely electromagnetic response, defined as RLC$_{electrode}$ is shown in green. A 1D electro-acoustic Mason model of the Pt/AlN/NbN stack (shown in red), including the electrode resistance and inductance of surrounding metallization, solving for the expected frequency range of BAW excitation. b) Measured return loss with a narrow 1 MHz step size revealing an underlying modulation of 12–13 MHz spacing between extrema, corresponding well to Fabry–Perot like interference with longitudinal thickness-modes of the 6 H–SiC substrate.

electrostatic capacitance, and inductance of the surrounding metallization. The measured insertion loss is well described by this purely electromagnetic response, but does not describe the observed oscillatory fringes. With the inductance of the surrounding metallization rather small, the resonators do not electromagnetically oscillate till well above 20 GHz.

Further inspection of the observed oscillatory fringes in the return loss, with a 1 MHz step size, are shown in Figure 4b. Under a narrower step size, the oscillatory fringes resolve as

modulations spaced 12–13 MHz apart. With the SiC substrate nearly 500 um thick, as measured by a micrometer, and taking the longitudinal acoustic wave velocity in SiC to be 13100 $m\,s^{-1}$,[17] the observed modulations in the measured return loss correspond to longitudinal BAW excitation in the AlN, which undergo Fabry–Perot like interference with longitudinal thickness-modes of the 6H–SiC substrate. This is the underlying operation principle of high overtone bulk acoustic resonators (HBAR) for the case in which the substrate is

significantly larger than the thin-film transducer stack, in which the spacing between neighboring resonances observed in the frequency domain, $\Delta f \approx v_{sub}/2L_{sub}$, where v_{sub} and L_{sub} correspond to the acoustic phase velocity and thickness of the substrate, respectively.[18]

A 1D electro-acoustic transmission line model along the c-axis of the Pt/AlN/NbN stack, commonly referred to as a Mason Model, was used to solve for the expected frequency range of BAW excitation under small signal RF excitation considering material parameters and layer thicknesses.[19,20] The calculated return loss of the fundamental bulk longitudinal mode from the Mason Model is shown in red in Figure 4a. Due to the finite thickness (mass load) of the Pt and NbN electrodes, f_0 was centered at about 8 GHz, instead of around 17 GHz that one might expect from considering the 330 nm AlN layer alone. For AlN-based resonators, the shift in resonant frequency and coupling coefficient due to electrode mass-loading becomes more prominent as operating frequencies approach 10 GHz, and strongly depends on the acoustic impedances of the top and bottom electrodes.[21] The model used here includes the electrode resistance and inductance of the surrounding metal, but not acoustical attenuation within the resonator or 6H–SiC substrate—providing an upper limit to the transduction process. The high electrode resistance (75 Ω) significantly broadens the expected electrical response of the AlN resonance. Within this broadened resonance, electromechanical transduction occurs, albeit weakly, over the 3 GHz to roughly 16 GHz observed in the measured S_{11}. Moreover, current studies of AlN, NbN, and 6H–SiC suggest the potential for all three materials to be acoustically matched with one another (≈ 41 MPa s m^{-3} for 6H–SiC,[4] ≈ 40 MPa s m^{-3} for NbN depending on the phase,[22] and ≈ 37 MPa s m^{-3} for AlN[4]). With the possibility for an acoustically transparent interface between the Pt/AlN/NbN thin-film stack and the substrate, a broadband response in the frequency domain is expected as the length of the cavity is greatly expanded.[18] Future studies are necessary to characterize the source(s) of acoustic loss in these films, both from the bulk growth, the interfaces, the etched AlN surface, and 6H–SiC substrate, as the measured response is weaker than one would expect considering the upper limit suggested by the model here. Furthermore, the acoustic attenuation of bulk 6H–SiC could be quite low ($\alpha \approx 4.6$ m^{-1} at 1 GHz[7]). Hence, with proper optimization of the NbN–6H–SiC interface, the epitaxial system studied here the potential to make a high-performing HBAR.

4. Conclusion

In this study, the strong etch of N-polar AlN in oxidizing solvents, such as KOH, was utilized to overcome the lack of dry etch selectivity between AlN and NbN. In the AZ400K etch, no visible signs of damage to the NbN were observed. In principle, a wet etch selective to AlN over NbN would provide a potential pathway to dramatically scale various nitride electronics—including BAW resonators—into the nanoscale regime while relieving dry etch constraints, and provokes further study of the AlN/NbN material system. The same chemistry damaged the active area when TMAH-based photolithographic developer was used to pattern

a photomask for metal deposition. A large portion of the electrode resistance can be attributed to this highly nonuniform Pt layer, a problem that could be avoided by growing a thin encapsulation layer on top of the AlN. Interestingly, a thin layer of NbN grown directly on AlN would simultaneously serve as an epitaxial electrode as well as an encapsulation layer for the electrode/piezoelectric interface, making the structure an all-epitaxial BAW. For applications that require the resonator to support exactly one excitation frequency, typically the substrate is etched from underneath the active area to strongly confine a single vibrational mode to within the AlN piezoelectric. Alternatively, a quarter-wavelength Bragg reflector, tuned to the resonant frequency, can be grown between the substrate and resonator cavity to achieve acoustic confinement.[21] For over a decade, the GaN monolithic microwave integrated circuit community has demonstrated "through substrate via" (TSV) process techniques on 6H–SiC substrates by controlled backside etching, enabling BAW technology to continue to deliver high-Q devices,even after switching to epitaxial AlN on 6H–SiC.[23–25] As piezoelectric and electrode thickness must scale together to achieve high-frequency BAW technology, epitaxial techniques of growing the electrode on both sides provide a means for maintaining thickness uniformity and high-quality interfaces down to the nanoscale. Moreover, such epitaxial growth techniques boast a family of exciting new structures directly applicable to the confinement and manipulation of phonons, such as compositionally graded stacks and superlattices. In addition to the growing interest in nanomechanical oscillators and superconducting devices for quantum computing and exploration of fundamental physics,[26–29] the use of NbN as an electrode presents a means of overcoming the tradeoff between electrode resistance and vibrational mode confinement one encounters at higher frequencies below the critical temperature, T_c, in which the NbN is superconducting.

Conflict of Interest

The authors declare no conflict of interest.

[1] S. Mahon, R. Aigner, in *CS Mantech Conf.*, Austin, TX **2007**, pp. 15–18.

[2] H. F. Tiersten, *J. Acoust. Soc. Am.* **1963**, *35*, 53.

[3] R. Vetury, M. D. Hodge, J. B. Shealy, in *2018 IEEE Int. Ultrasonics Symp. (IUS)*, Kobe, Japan **2018**, pp. 206–212.

[4] M. Rais-Zadeh, V. J. Gokhale, A. Ansari, M. Faucher, D. Theron, Y. Cordier, L. Buchaillot, *J. Microelectromech. Syst.* **2014**, *23*, 1252.

[5] R. Chaudhuri, S. J. Bader, Z. Chen, D. A. Muller, H. G. Xing, D. Jena, *Science* **2019**, *365*, 1454.

[6] J. Hasson, A. Many, *Phys. Rev. Lett.* **1975**, *35*, 792.

[7] R. Tabrizian, M. Rais-Zadeh, F. Ayazi, in *TRANSDUCERS 2009 Int. Solid-State Sensors, Actuators and Microsystems Conf.*, Denver, CO **2009**, pp. 2131–2134.

[8] D. J. Meyer, B. P. Downey, D. S. Katzer, N. Nepal, V. D. Wheeler, M. T. Hardy, T. J. Anderson, D. F. Storm, *IEEE Trans. Semicond. Manuf.* **2016**, *29*, 384.

[9] K. M. Lakin, J. Belsick, J. F. McDonald, K. T. McCarron, in *2001 IEEE Ultrasonics Symp. Proc. An International Symp.*, Vol. *1*, IEEE, Piscataway, NJ **2001**, pp. 827–831.

[10] K. Hashimoto, *RF Bulk Acoustic Wave Filters for Communications*, Artech House, Norwood MA **2009**.

[11] D. S. Katzer, N. Nepal, D. J. Meyer, B. P. Downey, V. D. Wheeler, D. F. Storm, M. T. Hardy, *Appl. Phys. Express* **2015**, *8*, 085501.

[12] R. Yan, G. Khalsa, S. Vishwanath, Y. Han, J. Wright, S. Rouvimov, D. S. Katzer, N. Nepal, B. P. Downey, D. A. Muller, H. G. Xing, D. J. Meyer, D. Jena, *Nature* **2018**, *555*, 183.

[13] W. Guo, R. Kirste, I. Bryan, Z. Bryan, L. Hussey, P. Reddy, J. Tweedie, R. Collazo, Z. Sitar, *Appl. Phys. Lett.* **2015**, *106*, 082110.

[14] D. Zhuang, J. H. Edgar, *Mater. Sci. Eng., R* **2005**, *48*, 1.

[15] L. Bin, M. Sun, T. Palacios, *IEEE Electron Device Lett.* **2013**, *34*, 369.

[16] H. H. Kim, B. K. Ju, Y. H. Lee, S. H. Lee, J. K. Lee, S. W. Kim, *Microelectron. Reliab.* **2004**, *44*, 237.

[17] K. Kamitani, M. Grimsditch, J. C. Nipko, C. K. Loong, M. Okada, I. Kimura, *J. Appl. Phys.* **1997**, *82*, 3152.

[18] S.-Y. Pao, M.-C. Chao, Z. Wang, C.-H. Chiu, K.-C. Lan, Z.-N. Huang, L.-R. Shih, C.-L. Wang, in *Proc. of the 2002 IEEE Int. Frequency Control Symp. and PDA Exhibition*, New Orleans, LA, **2002**, pp. 27–35.

[19] W. P. Mason, H. Baerwald, *Phys. Today* **1951**, *4*, 23.

[20] J. F. Rosenbaum, *Bulk Acoustic Wave Theory and Devices*, Artech House, Boston, MA **1988**.

[21] R. Lanz, P. Muralt, *IEEE Trans. Ultrason. Ferroelectr. Freq. Control* **2005**, *52*, 938.

[22] Y. Zou, X. Wang, T. Chen, X. Li, X. Qi, D. Welch, P. Zhu, B. Liu, T. Cui, B. Li, *Sci. Rep.* **2015**, *5*.

[23] M. Micovic, A. Kurdoghlian, H. P. Moyer, P. Hashimoto, A. Schmitz, I. Milosavljevic, P. J. Willadsen, W. S. Wong, J. Duvall, M. Hu, M. Wetzel, D. H. Chow, in *IEEE Compound Semiconductor Integrated Circuit Symp.*, IEEE, Piscataway, NJ **2005**, 3 pp.

[24] N. Okamoto, T. Ohki, S. Masuda, M. Kanamura, Y. Inoue, K. Makiyama, K. Imanishi, H. Shigematsu, T. Kikkawa, K. Joshin, N. Haral, in *CS Mantech Conf.*, Tampa, FL, May **2009**.

[25] F. A. Khan, I. Adesida, *Appl. Phys. Lett.* **1999**, *75*, 2268.

[26] M. Aspelmeyer, T. J. Kippenberg, F. Marquardt, *Rev. Mod. Phys.* **2014**, *86*, 1391.

[27] A. D. O'Connell, M. Hofheinz, M. Ansmann, R. C. Bialczak, M. Lenander, E. Lucero, M. Neeley, D. Sank, H. Wang, M. Weides, *Nature* **2010**, *464*, 697.

[28] M. V. Gustafsson, P. V. Santos, G. Johansson, P. Delsing, *Nat. Phys.* **2012**, *8*, 338.

[29] K. J. Satzinger, Y. P. Zhong, H. S. Chang, G. A. Peairs, A. Bienfait, M. H. Chou, A. Y. Cleland, C. R. Conner, É. Dumur, J. Grebel, *Nature* **2018**, *563*, 661.